

**COMPUTATIONAL ANALYSIS OF CRYSTAL GROWTH**

Final Report Contract No. NAS8-36483

CI-FR-0102

(NASA-CR-179027) COMPUTATIONAL ANALYSES OF  
CRYSTAL GROWTH Final Report (Continuum,  
Inc.) 63 p CSCI 20B

N87-20820

Unclas  
G3/76 45231

For

National Aeronautics and Space Administration  
George C. Marshall Space Flight Center  
Marshall Space Flight Center, AL 35812



From

**Continuum, Inc.**

Youssef M. Dakhoul

1500 Perimeter Parkway, Suite 125  
Huntsville, AL 35806-1686

January 1987

## **ACKNOWLEDGEMENTS**

This work is supported by NASA Contract NAS8-36483. The interest of the technical monitors, S. L. Lehoczky and F. R. Szofran is greatly appreciated.

## ABSTRACT

Two important aspects of Hg/Cd/Te crystal growth processes are discussed herein. First, the thermal field and, second the fluid movement in the melt zone. The thermal analysis includes numerical calculation of axisymmetric heat conduction within the sample. It also includes a three-dimensional radiation model to calculate the radiative heat exchange between the furnace and the crystal as determined by the complex geometry of the furnace and the adiabatic shield. The thermal analysis also includes a crystal conductivity which is dependent on temperature and composition. To tackle the fluid flow aspect of the problem, an attempt was made to use a newly developed incompressible flow code based on the slight compressibility, and hence the finite sound speed, of all real fluids.

**TABLE OF CONTENTS**

ACKNOWLEDGEMENTS ..... i

ABSTRACT ..... ii

TABLE OF CONTENTS ..... iii

INTRODUCTION ..... 1

INCOMPRESSIBLE FLOW CODE DEVELOPMENT ..... 3

RESULTS ..... 12

RECOMMENDATIONS ..... 13

REFERENCES ..... 14

APPENDIX A

## INTRODUCTION

This contract (NAS8-36483) started on April 24, 1985 with an intended period of performance of 12 months. During these first 12 months, a successful thermal analysis of Hg/Cd/Te crystal growth was performed. The analysis consisted of numerical axisymmetric heat conduction within the sample. A three-dimensional radiation model was incorporated to model the radiative heat exchange between the furnace and the crystal as determined by the complex geometry of the furnace and the adiabatic shield. The interface between the solid and melt phases was considered to be a non-isothermal surface determined by data from the phase diagram of the Hg/Cd/Te mixture. The conductivity in both the melt and solid phases was calculated as a function of temperature and composition. The objective of this phase was to determine the effect of furnace temperatures on the shape and location of the interface, and hence the quality and composition of the grown solid crystal. The effect of a metal tube enclosure on the thermal field within the crystal was also investigated. The results of this first phase of the study were completely documented and delivered to NASA as an interim report on May 1, 1986. A black and white copy of this report is included in Appendix "A" for the convenience of the reader.

As a result of the satisfactory completion of the first phase, the contract was extended to December 1986 to initiate a new phase of the study. This new phase is concerned with the fluid movement in the melt zone and its effect on the quality of the solid crystals.

Continuum, Inc. developed an incompressible flow code for use in a separate contract (NAS8-35508) as well as the second phase of this effort. The code incorporates a slight compressibility approach which takes advantage of the bulk modulus and finite sound speed of all real fluids. The finite element numerical analog uses a dynamic differencing scheme based, in part, on a variational principle for computational fluid dynamics. Details of the code's theory and calculation procedure are given in the following section.

The development and testing of the new code occupied most of the extended period of performance. An attempt was then made to use the code for calculating melt zone circulation. The attempt was unsuccessful because of two main reasons, namely, the extremely small magnitude of velocity compared to pressure, and the excessive amount of computational time required by the code. In other words, the approach is suitable for

relatively high speed flow regimes and requires expensive main-frame computer resources which were not available under this contract. The code was delivered to NASA under Contract NAS8-35508. Details of the theory and calculation procedure are given in the following sections, as well as conclusions and recommendations for future work.

## INCOMPRESSIBLE FLOW CODE DEVELOPMENT

### Nomenclature

a	-speed of sound
c	-incompressible specific heat
E	-total system energy
$E_B$	- bulk modulus of elasticity
F	-flux integrals, Eq. (14)
$\bar{I}$	-identity tensor
P	-pressure
$\bar{q}$	-velocity vector
$\bar{Q}$	-heat transfer
s	-entropy
t	-time
T	-temperature
u,v,w	- x-, y-, z- components of velocity, respectively
U	-conserved variable array, Eq. (14)
V	-volume
$\delta$	- artificial compressibility
$\mu$	- viscosity
$\nu$	- kinematic viscosity
$\xi$	- allocation parameters, Eq. (16)
$\rho$	- density
$\bar{\tau}$	- stress tensor

## Literature Review

The solution of the governing equations in primitive variable form for incompressible flows has proven to be a difficult task. The number of different equation sets used is nearly as large as the number of researchers working in the field. This is in sharp contrast to the solution of compressible gas flow in which, with the ideal gas assumption, the equations are well known. For incompressible gas and/or liquid flows, there is no comparable equation of state with which to close the system of equations. Density, and consequently pressure, are usually eliminated from the continuity equation, which becomes a constraint on the momentum equations. Although the pressure does appear in the momentum equations as spatial derivatives, neither of these equations can be solved for pressure without introducing directional bias (Ref. 1); nor can a transient type of solution be developed. Thus, from the outset one is faced with "N" equations for "N + 1" unknowns.

Early numerical solutions to incompressible flow avoided this problem by using the vorticity-stream function formulation, which is thoroughly treated in Ref. 1. This procedure suffers from many well known limitations, particularly for internal and three-dimensional problems (see, e.g., Refs. 1,2). With the realistic three-dimensional problems which are within reach by using current and future generations of supercomputers, the use of these equations will be severely limited.

One of the first procedures for obtaining pressures of incompressible flows required the solution of a Poisson equation (Ref. 1). This equation has the form

$$\nabla^2 P = S \quad (1)$$

where S is a non-linear function of the velocities and their first three derivatives. Also, Neumann boundary conditions are required to solve Eq. (1). The solution to Eq. (1) must be obtained iteratively at each step, a very time consuming process. Another drawback is that the solution does not behave well when complex geometries are being studied. Furthermore, the solution of Eq. (1) only once at each time step does not properly account for the velocity-pressure coupling, as demonstrated in Ref. 3. Since it is well known, Eq. (1) was specifically studied for inclusion into the crystal growth model;

however, because of the problems mentioned above, it was determined to be a non-viable alternative.

An increasingly popular solution used in finite difference applications is the artificial compressibility developed by Chorin (Ref. 4). This formulation assumes an equation of state as

$$P = \rho / \delta \quad (2)$$

where  $\delta$  is the artificial compressibility. Using Eq. (2) the continuity equation becomes

$$\delta \left( \frac{\partial P}{\partial t} \right) + \bar{\nabla} \cdot \bar{q} = 0 \quad (3)$$

Eq. (3) allows for an explicit finite difference solution for  $P$ ; however, since  $\delta$  is technically a relaxation parameter and has no physical basis, unsteady solutions are meaningless. Steady state solutions, on the other hand, have been obtained successfully by numerous researchers. Chang and Kwak (Ref. 5) and Kwak, et al (Ref. 6) present one of the most in depth and most successful applications of the method, including applications to SSME problems (Ref. 7).

A Finite Element Method (FEM) which embodies the same general principle as artificial compressibility is the penalty function formulation (Ref. 8). This procedure is widely used in pure FEM techniques, although many variants have been introduced in an attempt to obtain accurate results (for example, Refs. 9, 10). This further serves to illustrate the difficulty of obtaining pressures for incompressible flows.

The artificial compressibility method was considered for use in developing the crystal growth model, however, the essentially arbitrary nature of  $\delta$  in Eq. (3) creates several problems. Perhaps the major difficulty is in the use of the variational scheme explained later in this report. With no physical basis for  $\delta$ , the differencing procedure did not behave well. Other problems include the trial and error procedure required to determine  $\delta$ , and the unavailability of an unsteady solution.

There are numerous other methods for treating the velocity-pressure coupling, such as the transformed equations of Solomon and Szymczak (Ref. 11) or the assumed elemental "deviatoric stress-velocity-pressure" method of Yang and Atluri (Ref. 12). Few of these methods provide a set of physically accurate equations for the primitive variables. Also, transient problems can, at best, only be "studied" by iterating for successive steady state solutions, which is very costly and inefficient. Numerical damping is also necessary to obtain solutions in most of the available methods, including the artificial compressibility method.

A recently developed procedure which attempts to overcome most of these deficiencies is presented in Ref. 13. This work develops the pressure solution based on a finite sound speed, in other words, a compressible formulation. The compressibility is used to obtain an equation of state, which in turn introduces the pressure into the compressible form of the continuity equation. The resulting equation is

$$\frac{\partial P}{\partial t} + \bar{q} \cdot \bar{v} P + \rho c^2 (\bar{v} \cdot \bar{q}) = 0 \quad (4)$$

Eq. (4) has been successfully applied in Ref. 13 to both transient and high Reynolds number problems.

The procedure to be used in developing the crystal growth model is very similar to that of Ref. 13. The final equation differs somewhat from Eq. (4) because fewer assumptions will be made. The details of the analysis are presented below.

Basic Equations

In the development of the compressible formulation, the integral form of the equations of motion are used. Several advantages of this formulation occur, as pointed out in Ref. 14. The fundamental equations are:

continuity:

$$\iiint_{cv} \frac{\partial \rho}{\partial t} dV + \iint_{cs} \rho \bar{q} \cdot d\bar{s} = 0 \quad (5)$$

momentum:

$$\iiint_{cv} \frac{\partial \rho \bar{q}}{\partial t} dV + \iint_{cs} [(\rho \bar{q}) \bar{q} + (\bar{I}P - \bar{\tau})] \cdot d\bar{s} = 0 \quad (6)$$

energy:

$$\iiint_{cv} \frac{\partial \rho E}{\partial t} dV + \iint_{cs} [\rho E \bar{q} + (\bar{I}P - \bar{\tau}) \cdot \bar{q} + \bar{Q}] \cdot d\bar{s} = 0 \quad (7)$$

For this analysis, as with all incompressible methods, the assumption is made that  $P \neq P(T)$ , hence the energy equation (Eq. 7) decouples from the other equations. Since liquid flows are to be studied, it should also be pointed out that gravity, if assumed to be important, is easily included in Eq. (6) as a source term.

Pressure Solution

As previously discussed, the current approach to the pressure solution is to take advantage of the finite sound speed in all fluids, liquid or gas. The procedure is more correctly called a slight compressibility method, rather than an incompressible method.

An equation of state is assumed to exist in the form

$$P = P(\rho) \quad (8)$$

The compressibility of any fluid is expressed by the bulk modulus of elasticity,

$$E_B = \frac{dP}{\frac{d\rho}{\rho}} \quad (9)$$

and the finite acoustic speed in a liquid is given by

$$a^2 = \frac{E_B}{\rho} = \frac{dP}{d\rho} \quad (10)$$

The equation of state may now be written as

$$dP = a^2 d\rho \quad (11)$$

To derive the pressure equation, Eq. (11) is primarily used in differential form, however, a reference state must also be assumed for integration purposes. This reference state,  $P_r$  and  $\rho_r$ , must be assumed to be the usual theoretical incompressible values of  $P$  and  $\rho$  for the fluid being considered. Substitution of Eq. (11) into Eq. (5) now yields the pressure equation.

$$\iiint_{cv} \frac{\partial P}{\partial t} dV + \iint_{cs} P \bar{q} \cdot d\bar{s} + (\rho_r a^2 - P_r) \iint_{cs} \bar{q} \cdot d\bar{s} = 0 \quad (12)$$

The convective part of Eq. (12) is written as two terms to facilitate discussion of some salient features of the method. First, it should be noted that as the sound speed,  $a$ , approaches infinity (the true incompressible case) Eq. (12) reduces to the standard incompressible form of continuity. Another feature is that the artificial compressibility method can be viewed as a limiting case of Eq. (12). If the contribution of the pressure to the convective terms is discarded and  $\rho_r a^2 = 1/\delta$ , then Eq. (12) reduces to the integral form of Eq. (3). Perhaps the most important feature is the physical reasoning used to obtain Eq. (12). In addition to more correctly describing the physics of the flowfield, this method allows the use of a variationally based dynamic differencing scheme.

Eq. (11) could (and perhaps should) be included in the momentum equations. The error introduced by using  $\rho = \rho_r$  in Eq. (6) is essentially zero for steady state solutions, which can be viewed as incompressible solutions. For unsteady solutions, the error is of order  $\Delta P / \rho a^2$  vs.  $\rho$  and, since  $a$  is large, this error is assumed to be negligible.

### Numerical Analog

The numerical integration used to solve Eqs. (6) and (12) is based in part on the variational procedure developed by Prozan in Refs. 14-16. This procedure will be summarized below, and the application to the current work will then be discussed.

The compressible transport equations may be generalized as

$$\frac{\partial}{\partial t} \iiint_{cv} U_n dV = - F_n \quad ; \quad n = 1, \dots, 5 \quad (13)$$

where

$$U = \begin{Bmatrix} \rho \\ \rho \bar{q} \\ \rho E \end{Bmatrix} \quad ; \quad F = \iint_{cs} \left\{ \begin{array}{l} \rho \bar{q} \cdot d\bar{s} \\ [\rho \bar{q} \bar{q} + (\bar{I}P - \bar{\tau})] \cdot d\bar{s} \\ [\rho E \bar{q} + (\bar{I}P - \bar{\tau}) - \bar{q} + \bar{Q}] \cdot d\bar{s} \end{array} \right\} \quad (14)$$

Now, the domain of integration is subdivided into E finite elements and Eqs. (13) become

$$\sum_{e=1}^E (\Delta U_n \Delta V / \Delta t)_e = - \sum_{e=1}^E F_{n,e} \quad (15)$$

A functional distribution of the variables is assumed over the surfaces of the elements and the flux terms  $F_{n,e}$  are evaluated using values from the previous time step.

The  $(\Delta U_n \Delta V / \Delta t)_e$  represent the total accumulation of the nth conserved quantity within element e. To obtain the conserved variables at a new time step, nodes are placed at the corners of each element and the  $(\Delta U_n \Delta V / \Delta t)_e$  are allocated to the various nodes. Thus, the conserved quantities at the nodes are determined by assembling the contributions from its surrounding elements. This accumulation can be written

$$(\Delta U_n \Delta V / \Delta t)_j = - \sum_{e=1}^k \xi_{n,e,j} F_{n,e} \quad (16)$$

where j is the node number, k is the total number of elements surrounding node j, and the  $\xi_{n,e,j}$  are the allocation parameters.

The assembled equation, Eq. (16), is analogous to a finite difference expression in which the spatial transformations are numerically embedded in the analog. It may be interpreted as a general form of the finite difference scheme since different finite difference algorithms can be derived with selected allocation parameters. The variational differencing procedure differs from other schemes in that it does not dictate a fixed  $\xi_{n,e,j}$  throughout the course of integration, but rather, changes the parameters dynamically in both time and space according to the variational principle. This principle requires that the rate of entropy production be maximized. The variational differencing scheme thus uses the transport equations as equality constraints and dynamically determines the allocation parameters to achieve maximum stability of the system.

To apply the numerical analog to the current investigation, a procedure for determining the allocation parameters similar to the procedure of the Ref. 14 must be developed. A first attempt of this development was presented in Ref. 17. This method was not entirely satisfactory, and further research was performed. The entropy functional of Ref. 17 was further manipulated and the following derivatives were obtained:

$$\frac{\partial \rho s}{\partial P} = \frac{1}{a^2} c \ln T - c + \frac{1}{2} \frac{\bar{q}^2}{T} \quad (17)$$

where  $c$  is the specific heat,

$$\frac{\partial \rho s}{\partial \rho u} = - \frac{u}{T} \quad (18a)$$

$$\frac{\partial \rho s}{\partial \rho v} = - \frac{v}{T} \quad (18b)$$

$$\frac{\partial \rho s}{\partial \rho w} = - \frac{w}{T} \quad (18c)$$

Using Eqs. (17) and (18), the allocation parameters of Eq. (16) are determined in the same manner presented in Ref. 14. This procedure provided good stability for many cases.

## RESULTS

The results of the first phase of this study were completely documented and delivered to NASA as an interim report on May 1, 1986. A black and white copy of this report is included in Appendix "A" for the convenience of the reader. In the second phase of the project an attempt was made to use the newly developed incompressible code for calculating melt zone circulation. The attempt was unsuccessful for two main reasons. First, the velocity magnitude is so small that the numerical noise dominates the flowfield. To illustrate, consider the typical term  $(P + \rho u^2)$  which models the effect of pressure and inertial forces in the momentum equation. The velocity  $u$  is in the order of microns per second, while the pressure is in the order of  $10^6$  dyne/cm<sup>2</sup>. Thus, the round-off error in the pressure term may be larger than the magnitude of the cross-velocity term. It is therefore, impossible to calculate the velocity field without resorting to special procedures.

The second difficulty is the excessive amount of computational time required by the code. Since a realistic speed of sound in liquids (5000 ft/sec) must be used, the time step size required for stability is very small. The funds available for this project were not sufficient to secure any amount of main-frame computer resources to perform the required calculation.

The following conclusions have been arrived at:

1. The molten column is stable since it is heated from above and since the heavier material exists at the bottom of the column next to the interface.
2. The melt movement is due only to gravity which causes the liquid to "slide" along the curved interface.
3. The temperature and pressures inside the sample are much higher than the velocity magnitude.
4. Calculation of the velocity field in the molten crystal requires the development of a specialized code using an implicit rather than an explicit approach.

## RECOMMENDATIONS

It has been concluded that a strong effort should be devoted to developing a procedure for calculating the molten movement and its effect on the quality of the crystal. The following is a list of recommendations and guidelines for such an effort:

1. A "small perturbation" form of the governing equations must be used.
2. A thorough review of literature should be made to identify computer codes suitable for this kind of problems.
3. Effects of gravity, magnetic fields and density variations must be accurately accounted for.
4. An implicit algorithm must be developed to solve the governing equations.

## REFERENCES

1. Roache, P.J., Computational Fluid Mechanics, Hermosa Publishers, Albuquerque, N.M., 1982.
2. Gunzburger, M.D. and J.S. Peterson, "On the Finite Element Approximation of the Stream Function - Vorticity Equations," Advances in Computer Methods for Partial Differential Equations V, R. Vichnevetsky and R.S. Stepleman (eds.), IMACS, pp. 47-56, 1984.
3. Raithby, G.D. and G.E. Schneider, "Numerical Solution of Problems in Incompressible Fluid Flow: Treatment of the Velocity-Pressure Coupling," Num. Heat Transfer, Vol 2, pp. 417-440, 1979.
4. Chorin, A.J., "A Numerical Method for Solving Incompressible Viscous Flow Problems," J. of Computational Physics, Vol. 2, pp. 12-26, 1967.
5. Chang, J.L.C. and D. Kwak, "On the Method of Pseudo Compressibility for Numerically Solving Incompressible Flows," AIAA Paper 84- 252, January 1984.
6. Kwak, D., J.L.C. Chang, S.P. Shanks, and S. Chakravarthy, "A Three-Dimensional Incompressible Navier-Stokes Flow Solver Using Primitive Variables," AIAA J., Vol 24, No. 3, 1986.
7. Kwak, D., "Viscous Incompressible Flow Computation - A Summary of Recent Progress at Ames," SSME Computational Fluid Dynamics Fourth Working Group Meeting. Marshall Space Flight Center, AL, April 1986.
8. Hughes, T.J.R., W.K. Liu, and A. Brooks, "Finite Element Analysis of Incompressible Viscous Flows by the Penalty Function Formulation," J. of Computational Physics, Vol. 30, 1979, pp. 1-60.
9. Engleman, M.S., R.L. Sani, P.M. Gresho, and M. Bercovier, "Consistent vs. Reduced Integration Penalty Methods for Incompressible Media Using Several Old and New Elements," Int. J. Numerical Methods in Fluids, Vol 2, pp. 25-42, 1982.
10. Khashgi, H.S., and L.E. Scriven, "Variable Penalty Method for Finite Element Analysis of Incompressible Flow," Int. J. for Numerical Methods in Fluids, Vol 5, pp. 785-803, 1985.
11. Solomon, J.M. and W.G. Szymczak, "Finite Difference Solutions for the Incompressible Navier-Stokes Equations Using Galerkin Techniques," Fifth IMACS International Symposium on Computer Methods for Partial Differential Equations, Lehigh Univ., PA., June 1984.
12. Yang, C. and S.N. Atluri, "An Assumed Deviatoric Stress-Velocity-pressure Mixed Finite Element Method for Unsteady, Convective, Incompressible Viscous Flow: Part I: Theoretical Development," Int. J. for Numerical Methods in Fluids, Vol 3, pp. 377-398, 1983.

13. Kawahara, M. and Hirano, H., "A Finite Element Method for High Reynolds Number Viscous Fluid Flow Using Two Step Explicit Scheme," Int. J. for Numerical Methods in Fluids, vol. 3, pp. 137-163, 1983.
14. Prozan, R.J., "Hypothesis of a Variational Principle for Compressible Fluid Mechanics," CI-TR-0086, 1985.
15. Prozan, R.J., "A Variational Principle for Compressible Fluid Mechanics, Discussion of the One-Dimensional Theory," NASA CR-3526, April 1982.
16. Prozan, R.J., "A Variational Principle for Compressible Fluid Mechanics, Discussion of the Multi-Dimensional Theory," NASA CR-3614, October 1982.
17. Abernathy, J.M., and R. C. Farmer, "Computational Fluid Mechanics Utilizing the Variational Principle of Modelling Damping Seals," Interim Report, Contract NAS8-35508, NASA Marshall Space Flight Center, AL., 1985.

**APPENDIX A**

**SIMULATION OF MERCURY CADMIUM TELLURIDE CRYSTAL GROWTH**

Interim Report Contract No. NAS8-36483

For

National Aeronautics and Space Administration  
George C. Marshall Space Flight Center  
Marshall Space Flight Center, AL 35812



From

**Continuum, Inc.**

Youssef M. Dakhoul

4715 University Drive, Suite 118

Huntsville, AL 35816-3495

May 1, 1986

## **ACKNOWLEDGEMENTS**

This work is supported by NASA Contract NAS8-36483. The interest of the technical monitors, S. L. Lehoczky and F. R. Szofran is greatly appreciated.

## ABSTRACT

A thermal analysis of Hg/Cd/Te crystal growth in a Bridgman Cell is made using Continuum's VAST code and workstation facilities. The analysis consists of numerical axisymmetric heat conduction within the sample. A three-dimensional radiation model is incorporated to model the radiative heat exchange between the furnace and the crystal as determined by the complex geometry of the furnace and the adiabatic shield. The interface between the solid and melt phases is a non-isothermal surface determined by data from the phase diagram of the Hg/Cd/Te mixture. The conductivity in both the melt and solid phases is a function of temperature and composition. The objective of this study is to determine the effect of furnace temperatures on the shape and location of the interface, and hence the quality and composition of the grown solid crystal. The effect of a metal tube enclosure on the thermal field within the crystal is also investigated.

## TABLE OF CONTENTS

ACKNOWLEDGEMENTS .....	i
ABSTRACT .....	ii
TABLE OF CONTENTS .....	iii
TABLE OF FIGURES/TABLES .....	iv
INTRODUCTION .....	1
THERMAL PROPERTIES .....	2
THERMAL BOUNDARY CONDITIONS .....	7
INTERMEDIATE RESULTS .....	11
ADVANCED CALCULATIONS .....	18
FINAL RESULTS .....	21
CONCLUSIONS AND RECOMMENDATIONS .....	26
REFERENCES .....	27
APPENDIX A	

## TABLE OF FIGURES

Fig. 1	Properties of Air and Glass at Different Temperatures Data Supplied by NASA.....	3
Fig. 2	$Hg_{1-x}Cd_xTe$ Phase Diagram (Ref. 2) .....	5
Fig. 3	Schematic Presentation of the Boundary Conditions .....	8
Fig. 4	Geometry and Descretization (All Dimensions in mm) .....	12
Fig. 5	Effect of (THOT-TCOLD) on Thermal Gradients in the Sample .....	13
Fig. 6	Effect of TCOLD on Sample Isotherms.....	14
Fig. 7	A Closer Look at Interface Shape (Runs 6, 7 and 9) .....	15
Fig. 8	Effect of Translation Rate on Sample's Isotherms .....	17
Fig. 9	Determination of Interface Temperature and Solid Phase Composition .....	19
Fig. 10	Possible Shapes of Interface .....	19
Fig. 11	Sample's Isotherm and Compositions Under Different Cold Furnace Temperatures .....	22
Fig. 11 (Cont.)	Sample's Isotherms and Composition Under Different Cold Furnace Temperatures .....	23
Fig. 12	Details of Interface and Isotherms (Runs 16, 17 and 18) .....	24
Fig. 13	Effect of Metal Enclosure on Sample's Isotherms	

## TABLES

Table 1	Values of the Empirical Conductivity Coefficients (NASA) .....	6
Table 2	Values of the Phase Diagram's Empirical Constants (Ref. 2) .....	6

## INTRODUCTION

Mercury Cadmium Telluride crystals are essential for manufacturing infrared detection devices. The purity and composition uniformity of the crystal are most important and, unfortunately, difficult to achieve. The objective of this work is to identify methods and optimize conditions leading to the production of uniform and pure crystals.

This investigation specifically addresses the thermal phenomena which dominates the process of crystal growth. Numerical axisymmetric heat conduction within the Hg/Cd/Te sample is performed. The sample is regarded as consisting of a solid zone and a molten zone. The thermal conductivity in both zones is temperature and composition dependent. The interface between the two zones is taken in the first phase as the 706 °C isotherm, and in the second phase of the research is defined as a non-isothermal surface whose temperature distribution is obtained from the Hg/Cd/Te phase diagram. The composition in the solid zone is considered uniform if the interface is flat. If the interface is curved, the solid crystal composition is non-uniform in the radial direction and is taken from empirical data supplied by NASA. The heat exchange between the furnace and the sample, through the air gap and the glass ampule, is a complex phenomena of radiation and conduction. This exchanged heat is accurately calculated herein through a three-dimensional determination of the view factors, and a heat balance on the glass wall elements. Thus, the thermal energy flux at the sample's surface is determined and used as a boundary condition for solving the heat conduction equation within the sample's domain. The solution provides the thermal field within the sample and hence the shape of the interface and the composition distribution in the solid crystal. Parametric cases were calculated to study the effect of the furnace operating conditions and geometry on the quality of the crystals.

The following two sections of this report summarize the thermal properties and data used throughout the study, and the details of the boundary conditions calculation. Next, results of parametric cases (assuming isothermal interface) are presented. Finally, more advanced calculations of the interface's shape and the solid composition are presented followed by results of more parametric cases. At the end of the report, a list of conclusions and recommendations, a list of references and an appendix of mathematical details are attached.

## THERMAL PROPERTIES

The  $\text{Hg}_{1-x}\text{Cd}_x\text{Te}$  sample is assumed to have a constant density of  $7.45 \text{ gm/cm}^3$ . Density variations and convective motions in the molten zone are not considered in this study. The initial bulk composition,  $x_0$  is 0.2 for all the parametric cases presented herein. The density of the glass ampule is  $2.203 \text{ gm/cm}^3$  and its specific heat is  $1046.7 \times 10^6 \text{ mm}^2/\text{sec}^2 \text{ }^\circ\text{K}$ . The thermal conductivity of the ampule's glass,  $k_g$ , its radiative transmissivity,  $\tau$ , and the air's thermal conductivity,  $k_a$ , are all functions of temperature as shown in Fig. 1. The Stefan-Boltzmann constant is  $5.6696 \times 10^{-5} \text{ gm/sec}^3 \text{ }^\circ\text{K}^4$ , and the emissivities of all furnace surfaces are equal to 1.

The local composition,  $x$ , is calculated at each node in the liquid phase using the following one-dimensional species solution (1):

$$x = x_0 \left\{ 1 - \frac{S-1}{S} \exp(-RZ/D) \right\} \quad (\text{for } Z \geq 0)$$

where  $S$  is a segregation coefficient equal to 3.9;  $R$  is the growth rate (assumed equal to the translation rate);  $D$  is an effective diffusion coefficient equal to  $5.5 \times 10^{-5} \text{ cm}^2/\text{sec}$ ; and  $Z$  is the vertical distance above the interface whose location is defined later in this report. According to the above equation,  $x$  is equal to  $x_0/S$  at  $Z = 0$  and changes exponentially in  $Z$  to approach  $x_0$  as  $Z$  becomes large. In the solid phase ( $Z < 0$ ), the composition is first assumed constant and equal to  $x_0$ . In the last stage of this investigation, the solid composition is radially varied in a manner dependent on the shape of the interface. Details are given elsewhere in this report.

The thermal conductivity,  $K$ , is calculated at each node using the following equations (supplied by NASA):

$$K = \alpha \rho C_p$$

$$\alpha = A_0 - A_1 T^* + A_2 T^{*2} - A_3 T^{*3} \quad (\text{solid phase})$$

$$\alpha = B_0 \ln(T) - B_1 \quad (\text{liquid phase})$$

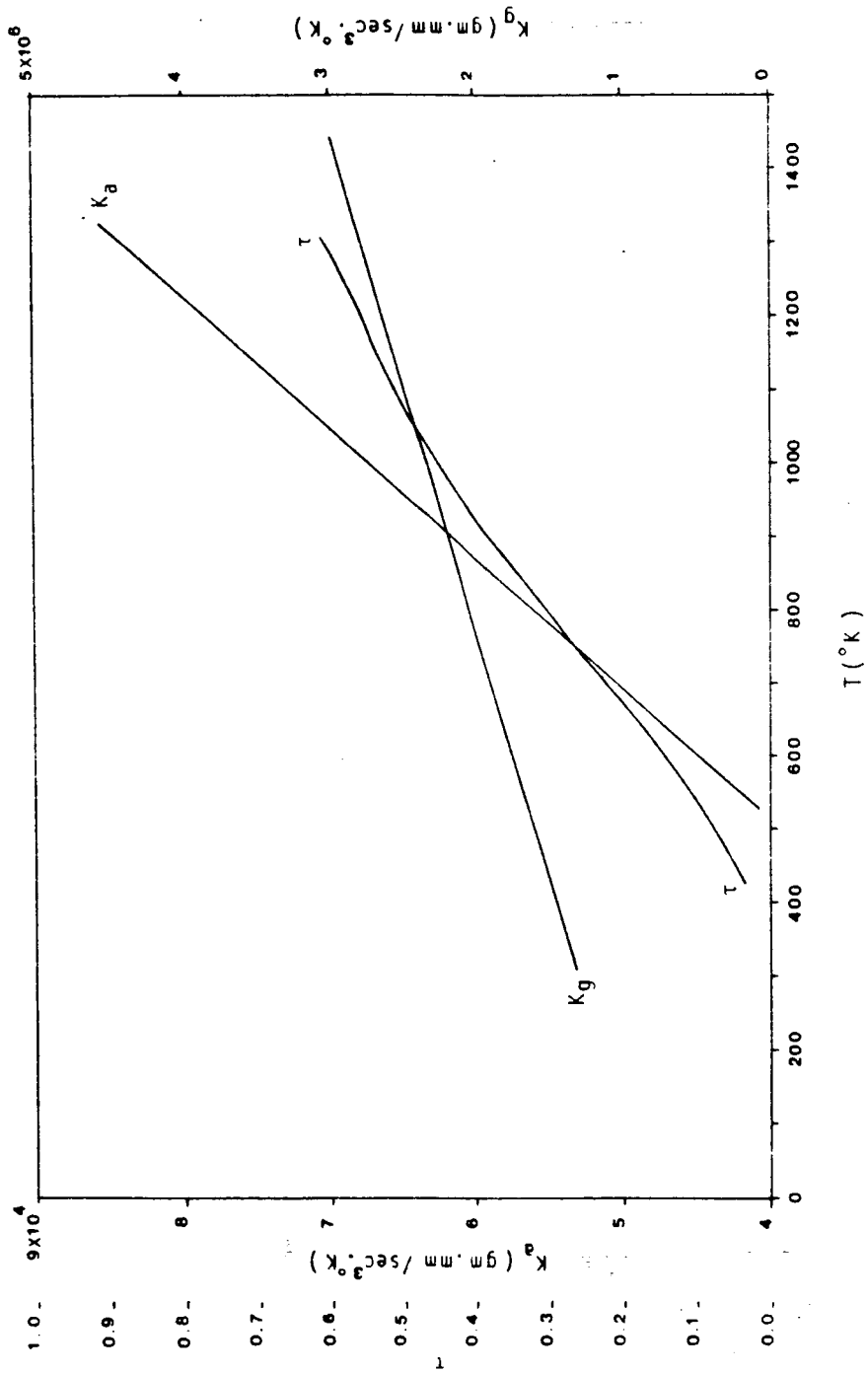


Fig. 1 Properties of Air and Glass at Different Temperatures.  
Data Supplied by NASA

where  $\alpha$  is the thermal diffusivity in  $\text{mm}^2/\text{sec}$ ;  $C_p$  is the heat capacity of the Hg Cd Te mixture (constant at  $1.8428 \times 10^6 \text{ cm}^2/\text{sec}^2 \text{ }^\circ\text{K}$ );  $T$  is the temperature in  $^\circ\text{C}$ ; and  $T^*$  is  $T/1000$ . The empirical constants,  $A_0, A_1, A_2, A_3, B_0,$  and  $B_1$  are given in Table 1 as functions of composition.

The pseudobinary phase diagram of Hg Cd Te mixtures, Fig. 2, is used herein for interface and solid composition determination as explained elsewhere in this report. The diagram is obtained from Ref. (2) and is described by the following empirical equations:

$$x^S = C_1 \sin\left(\frac{\pi}{2} T^*\right) + C_2 \sin\left(\frac{\pi}{2} \sqrt{T^*}\right) + C_3 \log_{10}(9 T^* + 1) \\ + C_4 \sqrt{T^*} \quad (\text{for } T \geq 690 \text{ }^\circ\text{C})$$

$$x^S = x_r^S (T - 670) / 20 \quad (\text{for } T < 690 \text{ }^\circ\text{C})$$

$$x^L = D_1 T^* + D_2 T^{*2} + D_3 T^{*3} + D_4 T^{*4}$$

where  $x^S$  is the solidus composition;  $x^L$  is the liquidus composition;  $T$  is temperature in  $^\circ\text{C}$ ; and  $T^*$  is equal to  $(T - 670)/412$ . The constants  $C_i$  and  $D_i$  ( $i = 1, \dots, 4$ ) are given in Table 2.

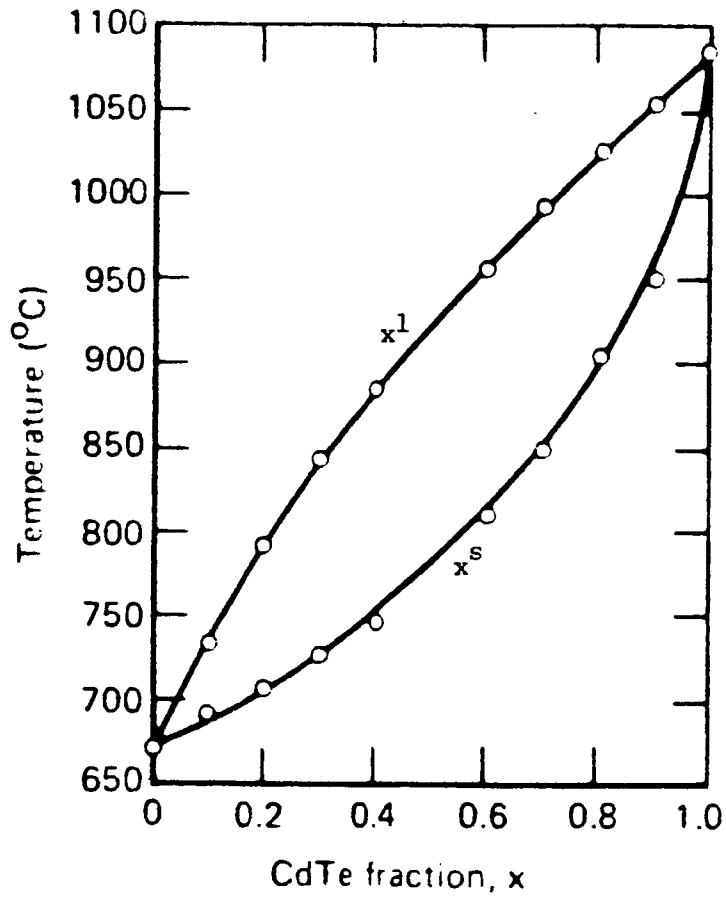


Fig. 2 Hg<sub>1-x</sub>Cd<sub>x</sub>Te Phase Diagram (Ref. 2)

<u>x</u>	<u>A<sub>0</sub></u>	<u>A<sub>1</sub></u>	<u>A<sub>2</sub></u>	<u>A<sub>3</sub></u>	<u>B<sub>0</sub></u>	<u>B<sub>1</sub></u>
0.000	2.784	9.938	20.98	16.21	10.4655	67.401
0.052	1.719	6.065	14.48	8.797	7.25493	46.767
0.107	1.512	6.494	14.81	11.03	7.09724	46.024
0.205	1.125	4.568	11.03	8.427	6.44051	42.041
0.301	1.031	4.652	11.59	8.933	5.69691	37.423

**Table 1 Values of the Empirical Conductivity Coefficients (NASA)**

<u>i</u>	<u>C<sub>i</sub></u>	<u>D<sub>i</sub></u>
1	0.502804	0.607640
2	0.165390	0.077209
3	0.746318	0.696167
4	-0.413546	-0.381683

**Table 2 Values of the Phase Diagram's Empirical Constants (Ref. 2)**

## THERMAL BOUNDARY CONDITIONS

Thermal energy is exchanged between the alloy and the furnace, through the glass wall of the ampule, by radiation and conduction. A part of the radiated energy is directly transmitted to the alloy while the glass wall absorbs the remaining part and reflects a negligible amount. The radiant energy absorbed by the glass, along with the energy conducted through the air gap, is conducted through the two-dimensional domain of the glass wall. A part of this conducted energy reaches the alloy, while the remaining part flows in the longitudinal direction. The net result is a certain amount of energy reaching or leaving the outer surface of the alloy per unit area per unit time. An accurate evaluation of this energy flux is vital for predicting a correct temperature distribution within the alloy. Once calculated, this energy flux,  $Q$ , can easily be used to impose the proper boundary condition on the solution of the energy equation.

In order to calculate the boundary heat flux,  $Q$ , a "lumped" heat balance is performed on the portion of the glass wall associated with each boundary node (see Fig. 3). This element of glass is assumed to have a uniform temperature  $T_a$  which is an average of the node temperature,  $T_n$ , and the temperature of the outer surface of the ampule at a point facing the node,  $T_g$ .  $T_n$  is obtained from the solution of the energy equation at the previous time iteration and  $T_g$  is calculated by equating the heat conducted to and through the air/glass interface:

$$(K_a / \delta_a) (T_f - T_g) = (K_g / \delta_g) (T_g - T_n)$$

where  $K_a$  and  $K_g$  are the conductivities of air and glass;  $\delta_a$  and  $\delta_g$  are widths of the air gap and glass wall; and  $T_f$  is the furnace temperature at a point facing the node. In a similar manner,  $T_{aa}$  and  $T_{ab}$  are calculated to represent average temperatures in the glass portions above and below the portion under consideration.

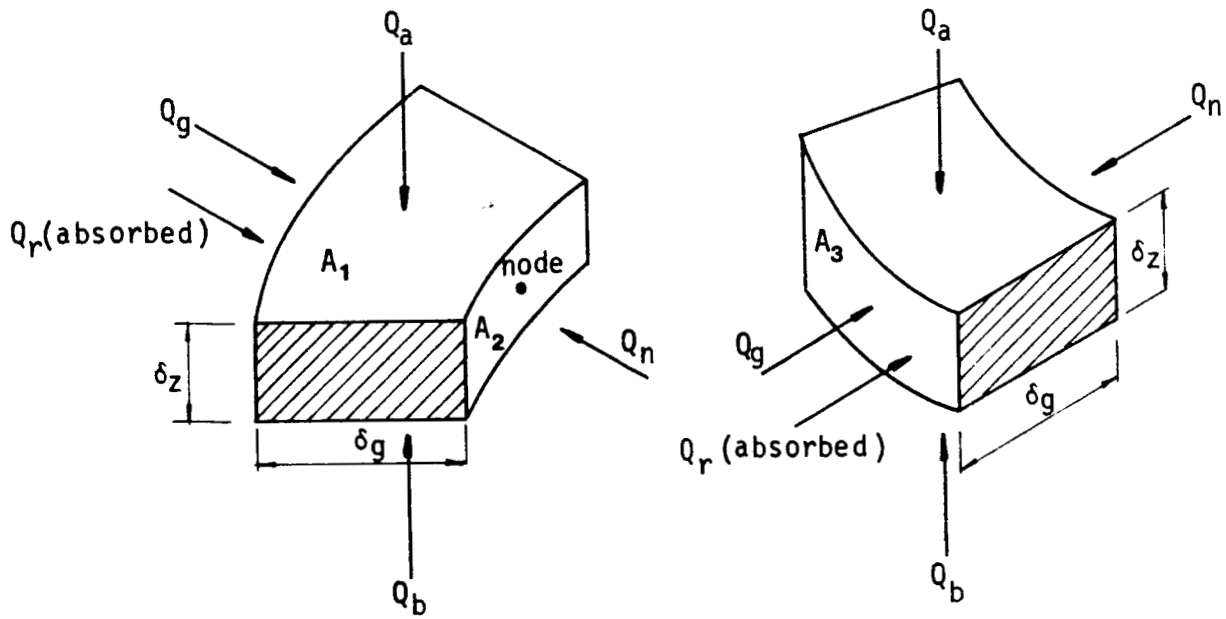
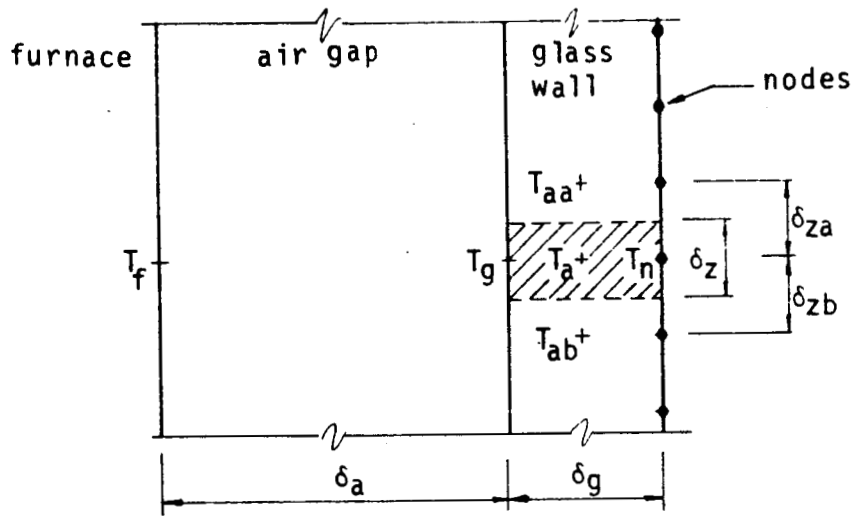


Fig. 3 Schematic Presentation of the Boundary Conditions

The set of temperatures  $T_f$ ,  $T_g$ ,  $T_a$ ,  $T_n$ ,  $T_{aa}$  and  $T_{ab}$  is used to calculate the following heat fluxes:

$$Q_a = (K_g / \delta_{za}) (T_{aa} - T_a)$$

$$Q_b = (K_g / \delta_{zb}) (T_{ab} - T_a)$$

$$Q_g = (2 K_g / \delta_g) (T_g - T_a)$$

$$Q_n = (2 K_g / \delta_g) (T_n - T_a)$$

$$Q_r(\text{absorbed}) = Q_r (1 - \tau)$$

$$Q_r(\text{transmitted}) = Q_r \tau$$

where  $\tau$  is the transmissivity of the glass, and  $Q_r$  is the radiative heat flux exchanged between the furnace and the glass element. Details for calculating  $Q_r$  are given in Appendix A. In each of the above formulae,  $K_g$  is the glass conductivity at a temperature equal to the average of the pair of temperatures used to calculate the flux. Also,  $\tau$  is the transmissivity of the glass at a temperature equal to  $(T_f + T_a)/2$ .

The above energy fluxes cause the temperature of the glass element to change from  $T_a$  to  $T_a'$ . The new  $T_a'$  is calculated from the heat balance on the glass "lump":

$$(V_g \rho_g C_g / \Delta t) (T_a' - T_a) = (Q_a + Q_b) A_1 + (Q_g + Q_r(\text{absorbed})) A_3 + Q_n A_2$$

where  $V_g$  is the volume of the glass element;  $\rho_g$  is the density of the glass;  $C_g$  is the specific heat of glass; and  $\Delta t$  is the time step size. The areas  $A_1$ ,  $A_2$  and  $A_3$  are shown in Fig. 3. Finally, the flux  $Q$  which represents the energy exchange between the furnace and the outer surface of the alloy in the vicinity of the node is calculated as:

$$Q = (2 K_g / \delta_g) (T_a' - T_n) + Q_r(\text{transmitted})$$

At each boundary node, the energy per unit volume  $\rho E_{old}$  (obtained by solving the energy equation) is adjusted to accommodate the flux  $Q$  as follows:

$$\rho E_{new} = \rho E_{old} + Q A_2 \Delta t/v$$

where  $v$  is the volume of the alloy element associated with the node. This energy adjustment is performed at the end of each time step.

## INTERMEDIATE RESULTS

The heat conduction equation is solved in the axisymmetric domain discretized as shown in Fig. 4. The thermal boundary condition at the wall nodes is as described in the preceding section. The temperature at the top end nodes is fixed at the hot furnace value, and the temperature of the bottom end nodes is equal to the cold furnace temperature. The interface is defined as the 706 °C isotherm. Thus, the molten and the solid zones are identified and separated by a sharp interface. The solid phase composition is constant at 0.2. Molten phase composition, and the conductivity of both phases are determined as described earlier.

Under the above conditions, 15 parametric cases are calculated. The first three cases are intended to show the effect of the difference between the hot and cold furnace temperatures (THOT-TCOLD) on the shape and distribution of the steady-state isotherms within the sample. It is easily seen in Fig. 5 that the sample's isotherms become closer to each other as the difference between THOT and TCOLD increases. In other words, a steeper temperature gradient across the heat barrier results in a steeper temperature gradient in the sample around the interface. The translation rate in all the three cases is 0.15  $\mu$ /sec.

Runs 4 through 11 are designed to investigate the effect of TCOLD on the location and hence, the shape of the interface. It is seen in Fig. 6 that the interface moves upward as TCOLD decreases while THOT is held constant. When the interface is in the lowest position (Run 4) it curves downward to become concave relative to the melt zone. As it moves upward, the interface flattens while TCOLD is in the range (425, 300 °C) and then curves upward to become convex relative to the melt zone as seen in Run 11. A closer look at the interfaces of Runs 6, 7 and 9 reveals, however, a subtle change in the interface curvature for the TCOLD range of (425, 300 °C). As seen in Fig. 7, the interface - while shifting steadily upwards as TCOLD falls - changes from concave to flat and then to concave again before it eventually becomes convex as in Runs 10 and 11. It is believed that the interplay between radiation, conduction and conductivity changes is responsible for this behavior of the interface. A detailed conceptual explanation is found in Ref. 1.

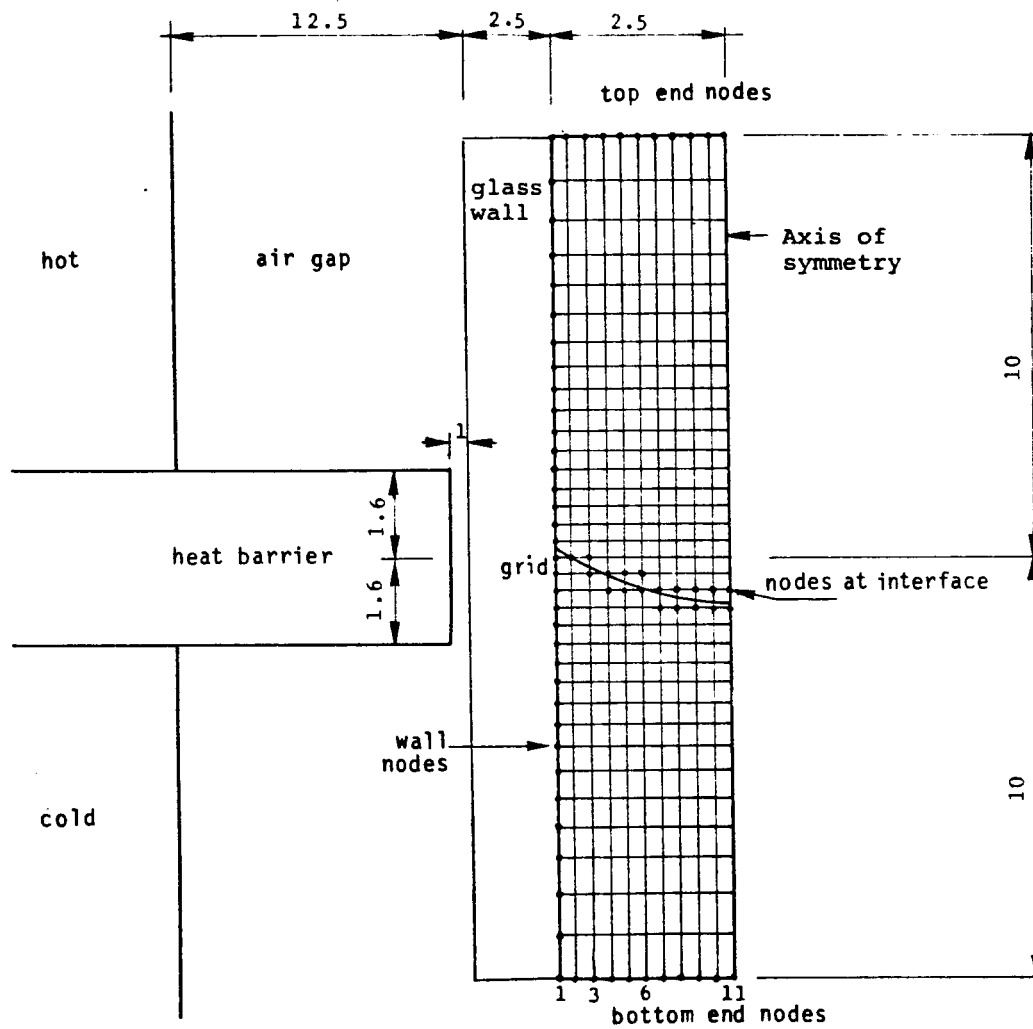


Fig. 4 Geometry and Descretization.  
 (All Dimensions in mm)

RUN # 1

THOT 784



2

812



3

859



TEMPERATURE  
AT  
STEADY STATE

806. °C  
756.  
706. INTRFC  
656.  
606.  
556.

CONTINUUM

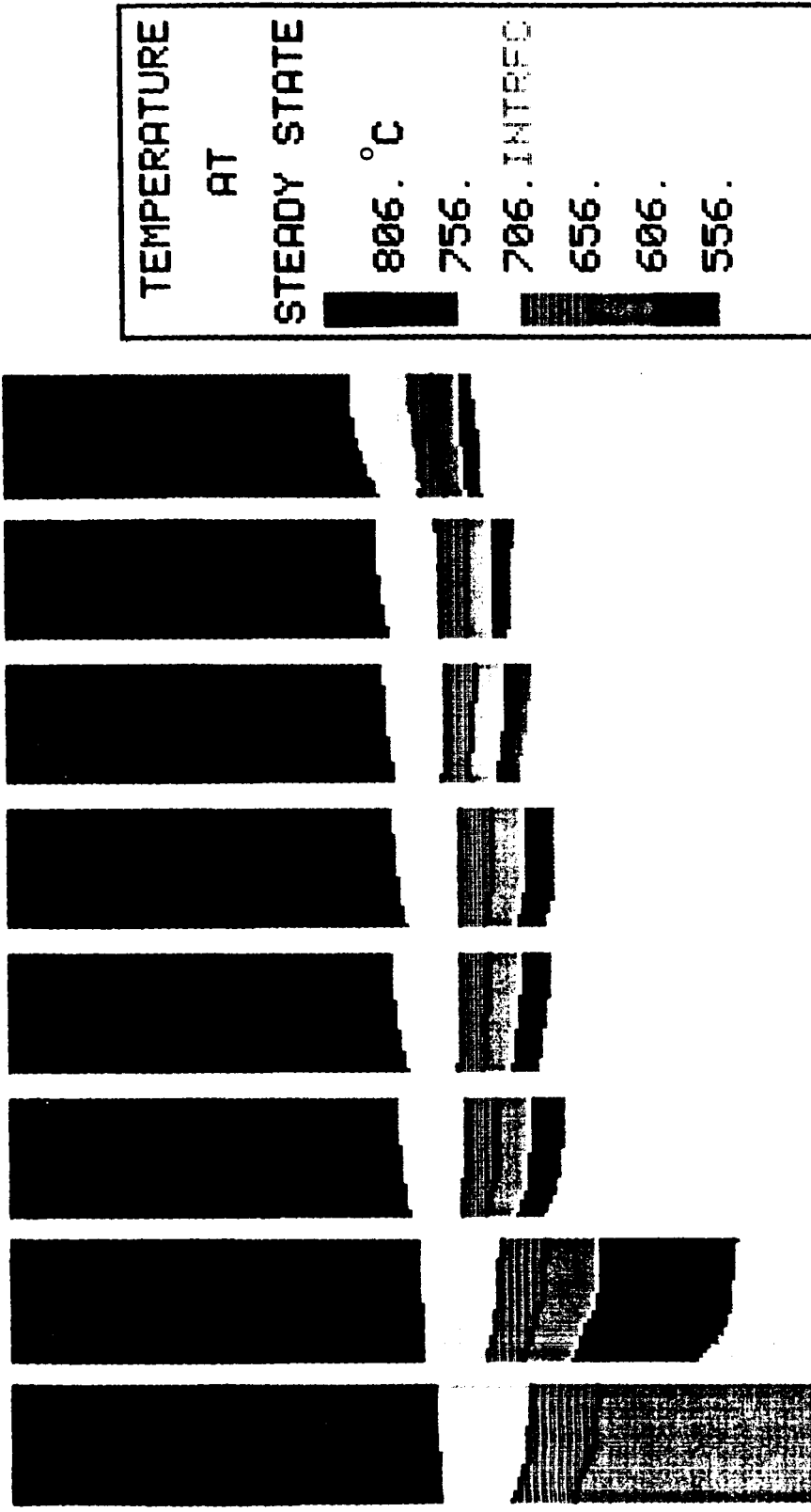
TCOLD 571

543

492

Fig. 5 Effect of (THOT - TCOLD) on Thermal Gradients in the Sample

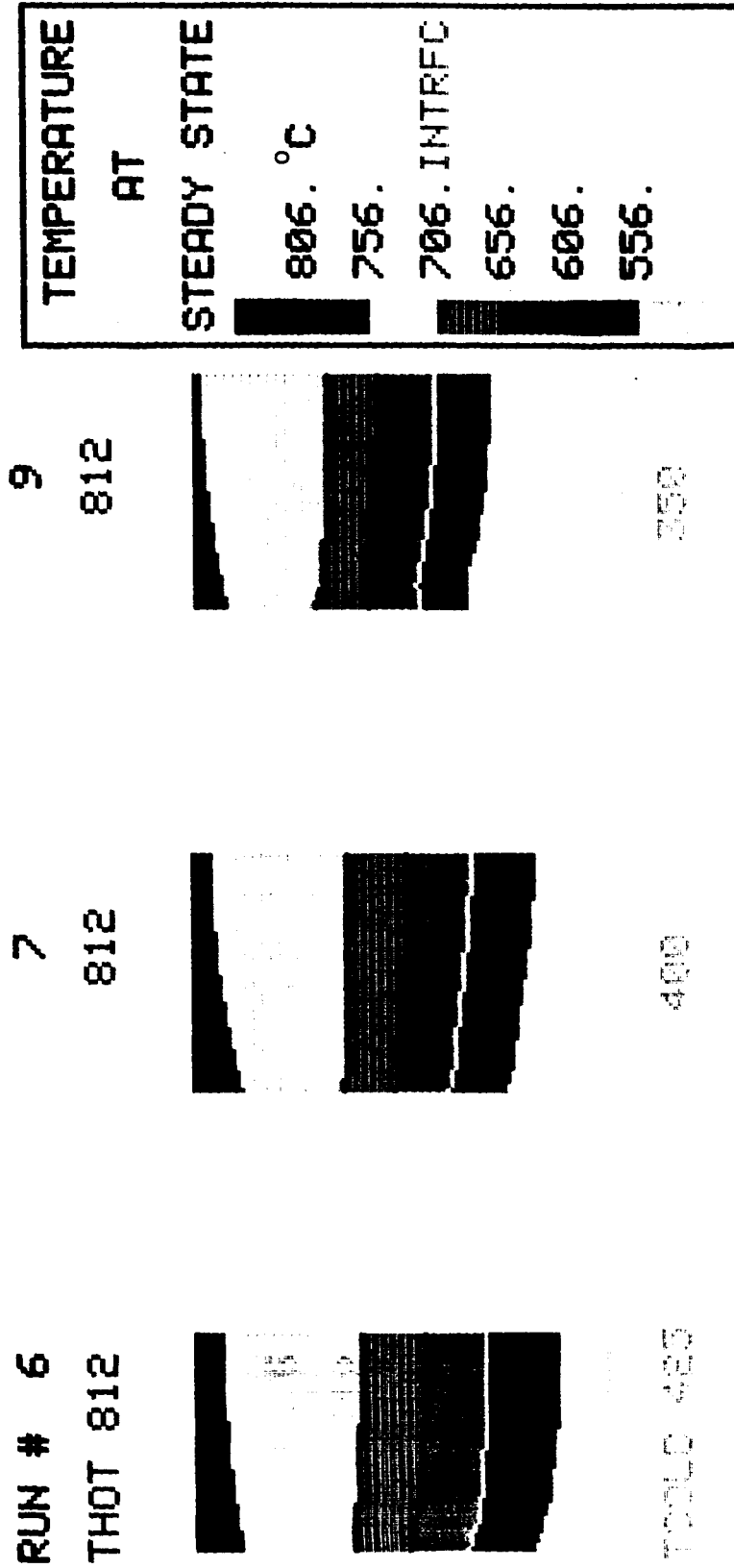
RUN#	THOT
4	812
5	812
6	812
7	812
8	812
9	812
10	812
11	812



CONTINUUM

519 343 425 400 375 350 320 100

Fig. 6 Effect of TCOLD on Sample Isotherms



CONTINUUM

Fig. 7 A Closer Look at Interface Shape  
(Runs 6, 7 and 9)

Runs 12 through 15 show the effect of the sample's translation rate on the steady-state isotherms and the shape and location of the interface. As seen in Fig. 8, the translation rate must be changed dramatically in order to cause a notable change in the distribution of the sample's isotherms.

ORIGINAL PAGE IS  
OF POOR QUALITY

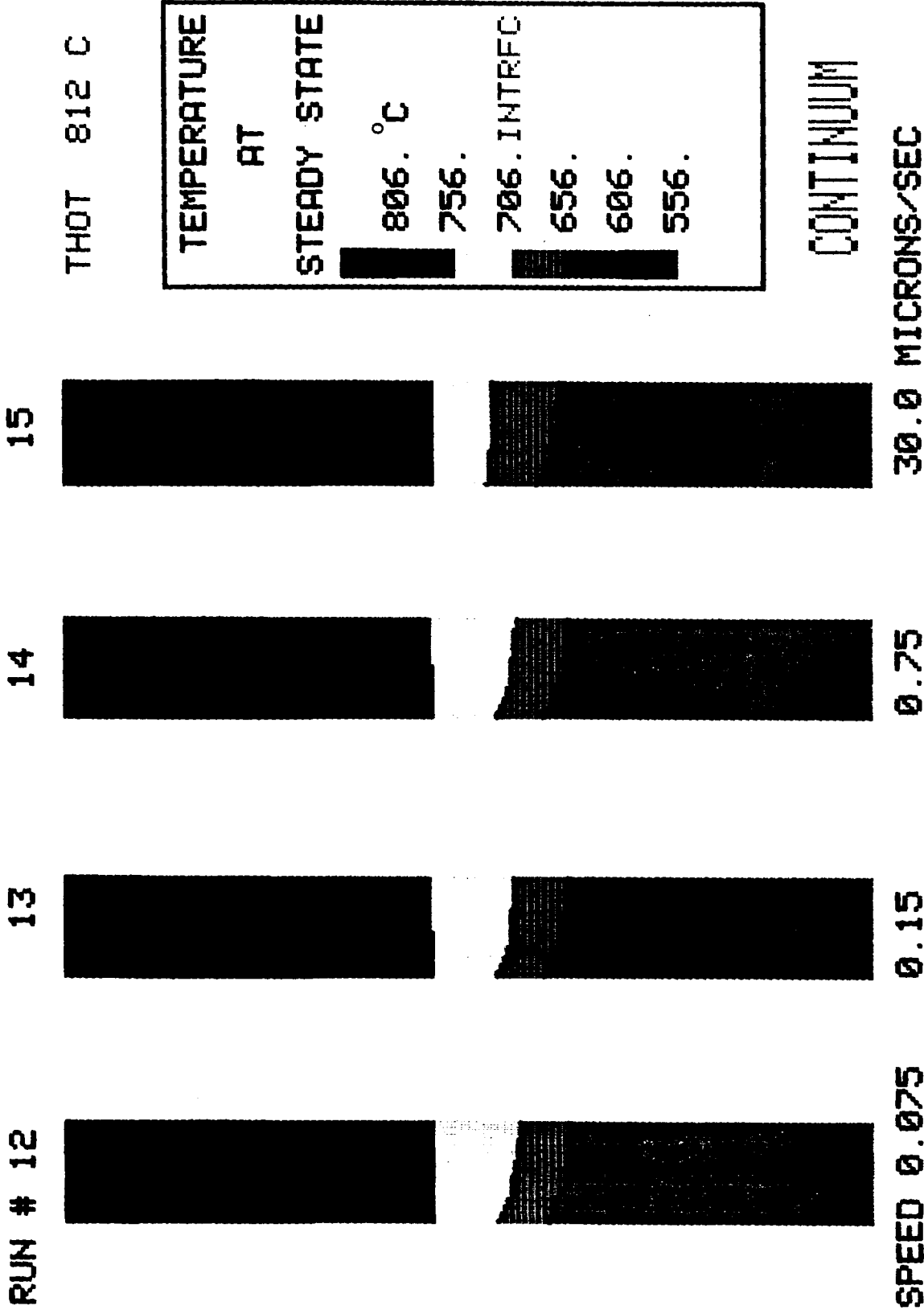


Fig. 8 Effect of Translation Rate on Sample's Isotherms

## ADVANCED CALCULATIONS

In this stage of the research, the interface is no longer considered as the 706 °C isotherm. Also, the solid phase composition is no longer fixed at the  $x_0$  value. The calculations of the melt phase composition and the thermal conductivity of both phases remain as explained earlier in this report.

Reference 3 presents a comprehensive empirical study of the solid crystal composition. Based on this study, it is herein assumed that the composition in the solid phase varies radially (and not axially) within the range (0.19, 0.235) for an initial bulk composition of 0.2. From the two composition values, 0.19 and 0.235, the temperature range within which solidification must have occurred is easily obtained from the phase diagram as shown in Fig. 9 (711.5, 702.5 °C). This temperature range is divided into ten segments which is equal to the number of elements used to discretize the sample in the radial direction (see Fig. 4). The set of temperatures  $T_1, T_2, \dots, T_{11}$  is then used to find the location of the interface on the axial planes passing through the corresponding nodes. For example, on the axial grid line number 6, the temperature of the interface is  $T_6$ . Hence, the location of the interface is easily determined by finding  $T_6$  on this axial grid line. Repeating the process over all the 11 grid lines, the interface is completely determined at the end of each time step.

If the interface is concave, as in Fig. 10(a), a disk of melt moving downwards will solidify first at the axial grid line number 1 at a temperature  $T_1$ . Thus, for the next time step, the interface is located by finding  $T_1$  on line number 1;  $T_2$  on line 2 and so on until  $T_{11}$  on line 11 which is the center line. In this case, the solid composition is assumed to vary from  $x_1$  (Fig. 9) at grid line number 1 to  $x_{11}$  at grid line 11.

If the interface is convex, as in Fig. 10(b), the molten disk moving downwards will solidify first at the axial grid line number 11 under a temperature of  $T_1$ . Thus, for the next time step, the interface is located by finding  $T_1$  on line number 11;  $T_2$  on line number 10 and so on until  $T_{11}$  on line number 1. In this case, the solid composition varies from  $x_1$  at grid line number 11 to  $x_{11}$  at grid line 1.

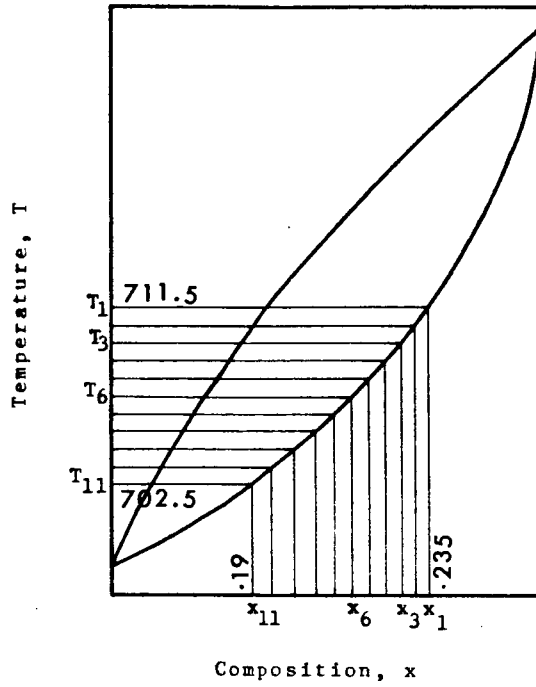


Fig. 9 Determination of Interface Temperature and Solid Phase Composition

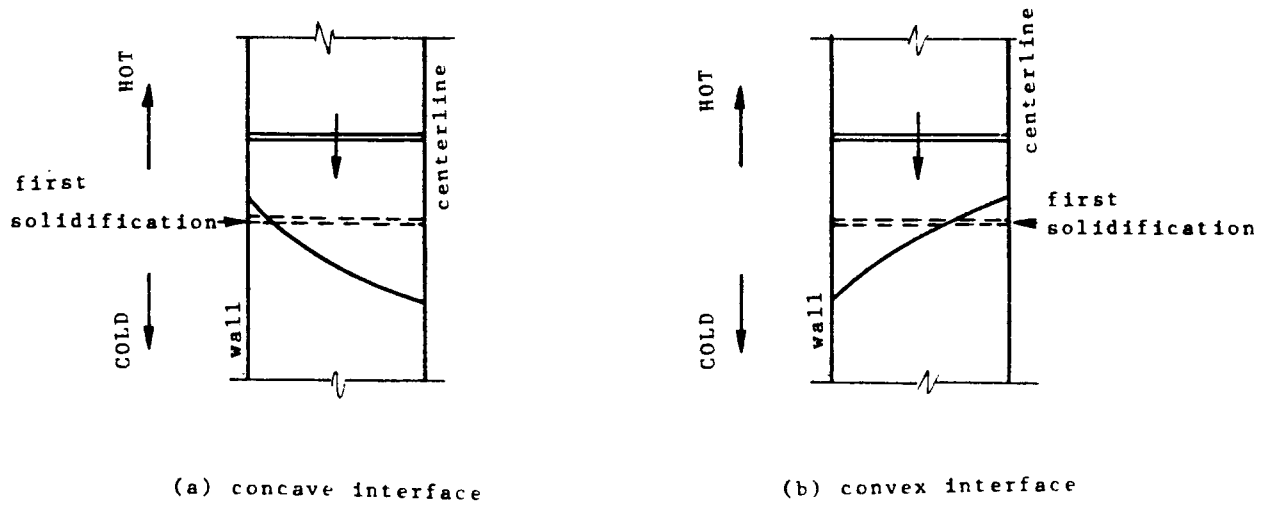


Fig. 10 Possible Shapes of Interface

The interface is flat when the set of temperatures  $T_1, T_2, \dots, T_{11}$  all lie on a horizontal line within certain tolerance. In this case the solid composition is uniform at 0.2.

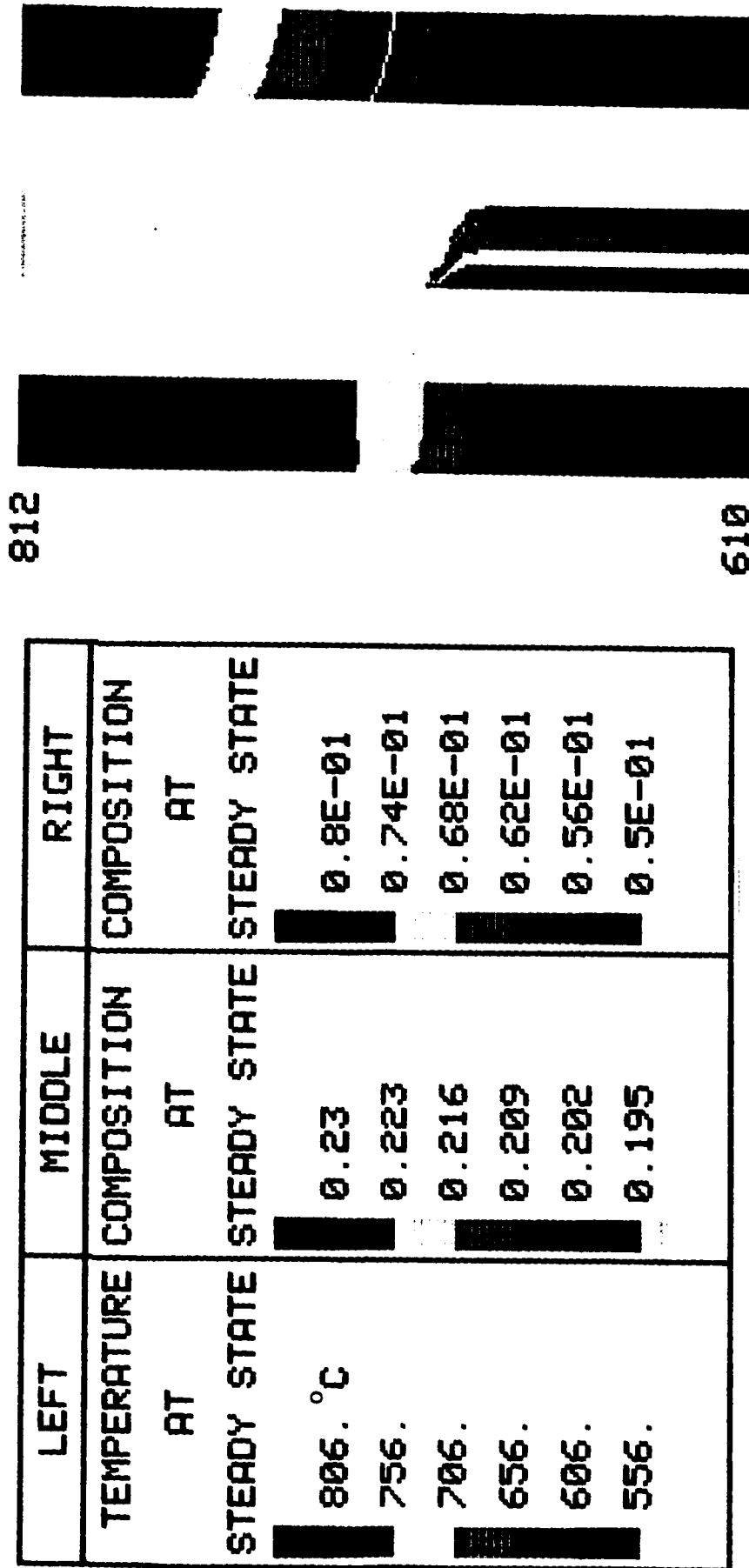
## FINAL RESULTS

Six parametric cases (Runs 16 through 21) are calculated under the conditions mentioned in the preceding section. In runs 16, 17 and 18, THOT is 812 °C and TCOLD is 610, 350, and 75 °C respectively. The translation rate in all the three runs is 0.15 μ/sec. Figure 11 shows the effect of TCOLD on the shape of the sample's isotherms and on the composition distribution in both the molten and solid phases. Figure 12 is a detailed view of the isotherms in the solidification zone with the non-isothermal interface shown as a dashed line. It is seen that if THOT is fixed at 812 °C, a TCOLD of 350 °C is required to produce a flat interface and, hence, a uniform composition in the solid crystal. A numerical optimization tool for Hg Cd Te crystal quality control is thus created. Runs similar to 16, 17 and 18 can be easily used to predict the quality of the grown crystals under a variety of furnace operating conditions and geometries.

Runs 19, 20 and 21 differ from the three preceding runs in that the glass ampule is enclosed in a metal tube of 12.94 mm diameter. The disk-like heat barrier surrounds this metal tube on the outside and ensures that the temperature distribution along the tube is identical to that of the furnace. Thus, the procedure for calculating the radiative heat flux at the sample's boundary remains the same. Only the furnace is now at the position of the metal tube and the heat barrier is absent.

Figure 13 shows the results of Runs 19, 20, 21 compared to those of Runs 16, 17, 18. It is seen that the effect of the metal tube is to bring the isotherms at the sample's boundary closer together. That is expected since, in effect, the furnace was moved closer to the sample forcing its temperature distribution to follow more closely that of the furnace. Note also that in order to obtain a flat interface, a TCOLD of 400 °C is needed instead of 350 °C.

RUN # 16

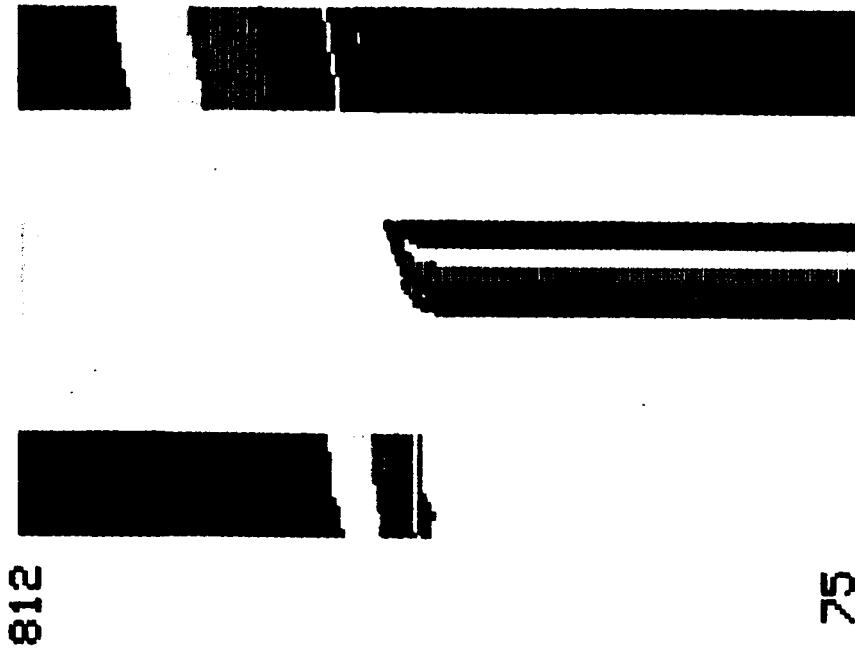


CONTINUUM

Fig. 11 Sample's Isotherm and Compositions Under Different Cold Furnace Temperatures

ORIGINAL PAGE IS  
OF POOR QUALITY

RUN # 18



RUN # 17

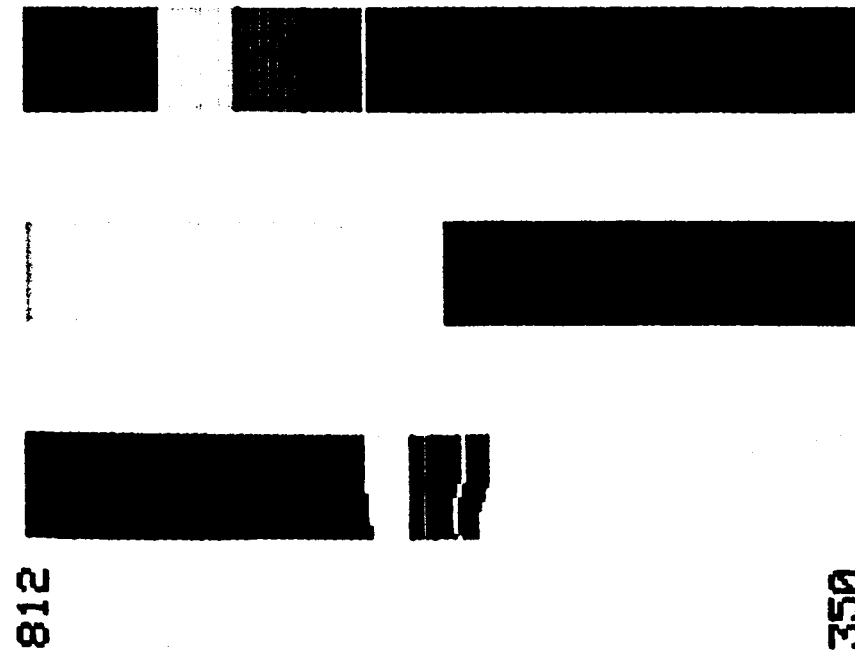


Fig. 11 (Cont.) Sample's Isotherms and Composition  
Under Different Cold Furnace Temperatures

CONTINUUM

ORIGINAL PAGE IS  
OF POOR QUALITY

TEMPERATURE	AT
806.	°C
756.	
706.	
656.	
606.	
556.	

18

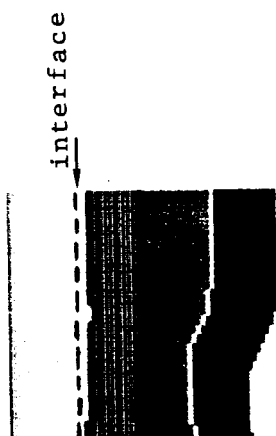
812



706

17

812



706

RUN # 16

THOT 812



706

CONTINUUM

Fig. 12 Details of Interface and Isotherms  
(Runs 16, 17 and 18)

ORIGINAL PAGE IS  
OF POOR QUALITY

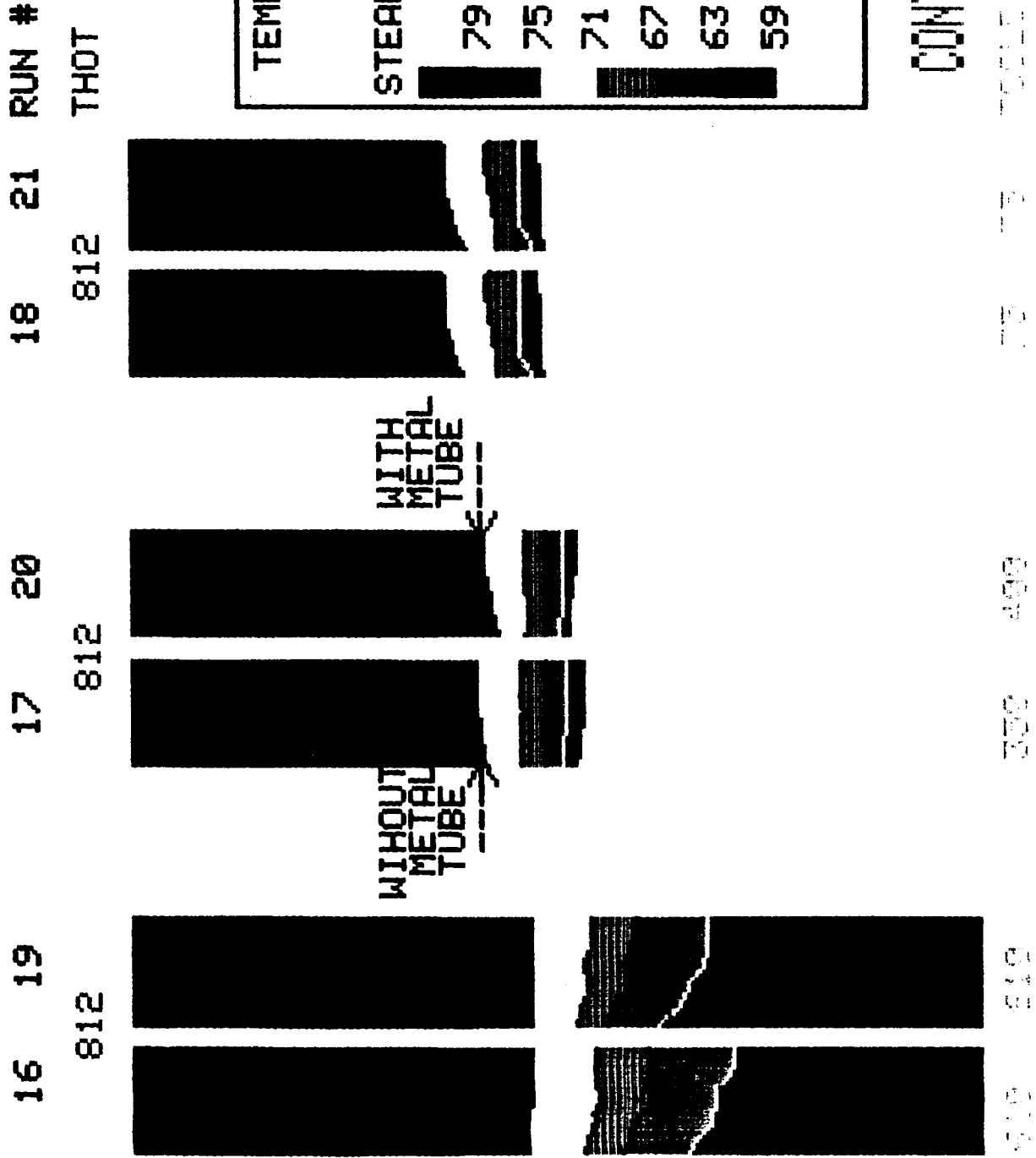


Fig. 13 Effect of Metal Enclosure on Sample's Isotherms

## CONCLUSIONS AND RECOMMENDATIONS

An accurate thermal analyzer of Hg Cd Te crystal growth was developed which includes the following aspects:

- a. Axisymmetric heat conduction in the sample.
- b. Three-dimensional calculation to model the radiative heat exchange between the furnace and the crystal as determined by the complex geometry of the furnace and the adiabatic shield.
- c. Non-isothermal interface between the solid and molten phases determined by the phase diagram of the Hg Cd Te mixture.
- d. Temperature and composition dependent conductivity in both the melt and solid regions.

The model was used to investigate the effect of the furnace temperature distribution, and the translation rate on the location and shape of the interface and, hence, on the quality of the grown crystal as indicated by its composition distribution. Also, the effect of a metal tube enclosure was investigated. The results are displayed in Figs. 5 through 13 and discussed earlier in this report. The model can be systematically used to predict the quality of the crystal grown under different conditions.

It is recommended that a new phase of the study be started to add the following attributes to the model:

- a. The fluid mechanics of the motion of the dense liquid in the molten zone; its effect on the shape of the interface and the quality of the grown crystal.
- b. Effect of gravity (or its absence) on the fluid motion.
- c. Effect of any magnetic field that may exist and affect the flow in the melt zone.

## REFERENCES

1. Szofran, F. R. and S. L. Lehoczky, "A Method for Interface Shape Control During Bridgman Type Crystal Growth of Hg Cd Te Alloys", Space Science Laboratory Preprint Series No. 84-132, May 1984.
2. Szofran, F. R. and S. L. Lehoczky, "The Pseudobinary Hg Te-Cd Te Phase Diagram", J. Electronic Materials, Vol. 10, p. 1131, 1981.
3. Lehoczky, S.L. and F.R. Szofran, "Directional Solidification and Characterization of  $\text{Hg}_{1-x}\text{Cd}_x\text{Te}$  Alloys", in Materials Processing in the Reduced Gravity Environment of Space, Edited by G. E. Rindone, Elsevier Science Publishing Company, P. 409-420, 1982.

**APPENDIX A**

**BASIC CALCULATION FOR RADIATIVE EXCHANGE**

The basic expression for the radiative exchange between the furnace and a certain location within the glass or the alloy's surface can be written as follows:

$$q_{dA_f \rightarrow dA_n} = \epsilon_f \sigma T_f^4 F_{dA_f \rightarrow dA_n} dA_f - \epsilon_n \sigma T_n^4 F_{dA_n \rightarrow dA_f} dA_n. \quad (A-1)$$

This is the net energy diffusely leaving the differential area  $dA_f$  and reaching the differential area  $dA_n$  per unit time (see figure A-1). It is assumed that the media between  $dA_f$  and  $dA_n$  does not participate in the radiation process. A negative quantity means that the net energy leaves  $dA_n$  and reaches  $dA_f$ .  $\sigma$  is the Stefan-Boltzmann constant;  $(\epsilon_f, T_f)$  and  $(\epsilon_n, T_n)$  are emissivities and temperatures of  $dA_f$  and  $dA_n$  respectively. The view factors between the two differential areas are given by:

$$F_{dA_f \rightarrow dA_n} = \cos\phi_f \cos\phi_n dA_n / \pi S^2, \quad (A-2)$$

$$F_{dA_n \rightarrow dA_f} = \cos\phi_f \cos\phi_n dA_f / \pi S^2, \quad (A-3)$$

where  $S$  is the distance between the two differential areas;  $\phi_f$  and  $\phi_n$  represent the angles between the line  $S$  and the normals to  $dA_f$  and  $dA_n$  respectively. If  $(R_n, \theta_n, z_n)$  and  $(R_f, \theta_f, z_f)$  are the cylindrical coordinates of the centers of  $dA_n$  and  $dA_f$  respectively, the following expressions are easily obtainable:

$$dA_f = R_f d\theta_f dz_f, \quad (A-4)$$

$$dA_n = R_n d\theta_n dz_n, \quad (A-5)$$

$$S^2 = R_f^2 - 2 R_f R_n \cos(\theta_f - \theta_n) + R_n^2 + (z_f - z_n)^2, \quad (A-6)$$

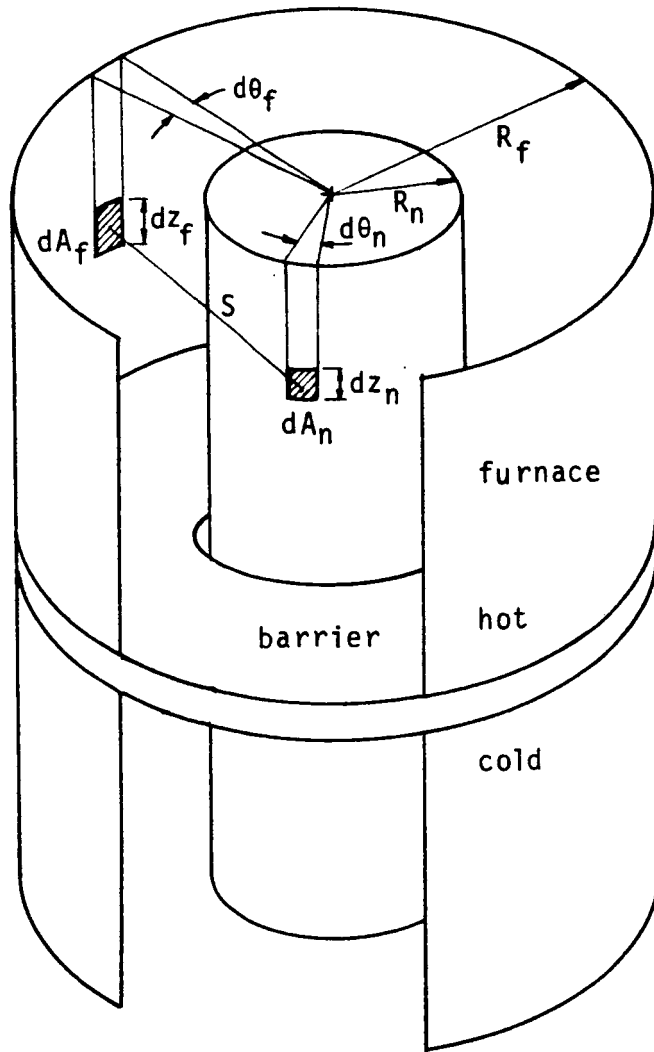


Fig. A-1: Radiation Heat Transfer

$$\cos \phi_f = (1/S) [R_f - R_n \cos(\theta_f - \theta_n)] , \quad (\text{A-7})$$

$$\cos \phi_n = (1/S) [R_f \cos(\theta_f - \theta_n) - R_n] . \quad (\text{A-8})$$

Using Equations (A-2) through (A-8), Equation (A-1) is rewritten as:

$$q_{dA_f \rightarrow dA_n} = \Omega_1 \Omega_2 \Omega_3 d\theta_n dz_n d\theta_f dz_f , \quad (\text{A-9})$$

where  $\Omega_1$ ,  $\Omega_2$  and  $\Omega_3$  are given by:

$$\Omega_1 = R_n R_f \sigma / \pi , \quad (\text{A-10})$$

$$\Omega_2 = \frac{[R_f \cos(\theta_f - \theta_n) - R_n] [R_f - R_n \cos(\theta_f - \theta_n)]}{[R_f^2 - 2 R_n R_f \cos(\theta_f - \theta_n) + R_n^2 + (z_f - z_n)^2]^2} , \quad (\text{A-11})$$

$$\Omega_3 = \epsilon_f T_f^4 - \epsilon_n T_n^4 . \quad (\text{A-12})$$

Now, suppose that  $A_f$  is the finite furnace area "seen" by  $dA_n$ . As shown in Figure A-2,  $A_f$  consists of two separate regions on the outer cylinder plus the vertical edge of the heat barrier. Depending on the location of  $dA_n$ , the area  $A_f$  may also include one of the horizontal surfaces of the barrier. The outer cylinder portions of  $A_f$  consist of a collection of elemental areas similar to  $dA_f$  of Figure A-1. Thus, the radiative exchange between this portion of  $A_f$  and  $dA_n$  is described by equations (A-4) through (A-12). The heat barrier portions of  $A_f$ , on the other hand, consist of elemental areas having variable  $R_f$  and different orientations with respect to  $dA_n$ . Thus, Equations (A-4) and (A-7) should be rewritten for these elemental areas on the heat barrier. This can be avoided by realizing that the radiation exchange between  $dA_n$  and  $dA_f'$  (see Figure A-3) is equal to

that between  $dA_n$  and  $dA_f$  if  $dA_f'$  and  $dA_f$  have the same thermal properties. That is because  $dA_n$  "sees"  $dA_f'$  and  $dA_f$  through the same solid angle. Thus, the horizontal surface of the barrier can be replaced by the outer cylinder region lying between points A and B in Figure A-3. It must be kept in mind that each element  $dA_f$  in this region must be given the same thermal properties as its  $dA_f'$  counterpart. In a similar manner, the vertical edge of the heat barrier can be replaced by the region BC on the outer cylinder.

The net energy exchange, per unit time, between a finite area,  $A_n$ , on the inner cylinder and the furnace area,  $A_f$ , seen by it can now be obtained by integrating Equation (A-9) over  $A_n$  and  $A_f$ :

$$q_{A_f \rightarrow A_n} = \int_{A_f} \int_{A_n} \Omega_1 \Omega_2 \Omega_3 d\theta_n dz_n d\theta_f dz_f . \quad (\text{A-13})$$

A positive result means that the energy leaves  $A_f$  and reaches  $A_n$ , while a negative value indicates a net energy loss from  $A_n$  to  $A_f$ . The area  $A_n$  is described by the ranges  $(\theta_{n,1} \rightarrow \theta_{n,2})$  and  $(z_{n,1} \rightarrow z_{n,2})$ . Also,  $A_f$  is defined by  $(\theta_{f,1} \rightarrow \theta_{f,2})$  and  $(z_{f,1} \rightarrow z_{f,2})$ . Since the boundary nodes are arranged on the alloy's surface with a  $\theta$  interval of 1 rad and a small vertical interval,  $\Delta z_n$ , it is convenient to write:

$$\theta_{n,1} = 0 , \quad (\text{A-14})$$

$$\theta_{n,2} = 1 , \quad (\text{A-15})$$

$$z_{n,2} - z_{n,1} = \Delta z_n . \quad (\text{A-16})$$

Also, as seen in Figure A-4,  $\theta_{f,1}$  and  $\theta_{f,2}$  are defined for each value of  $\theta_n$  as follows:

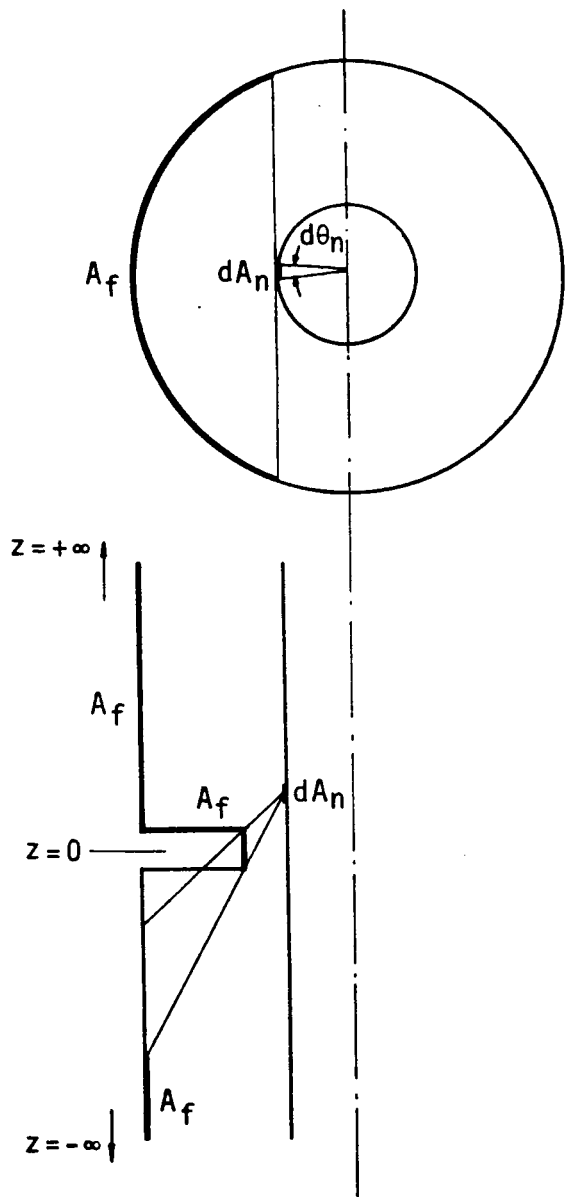


Fig. A-2: Furnace View

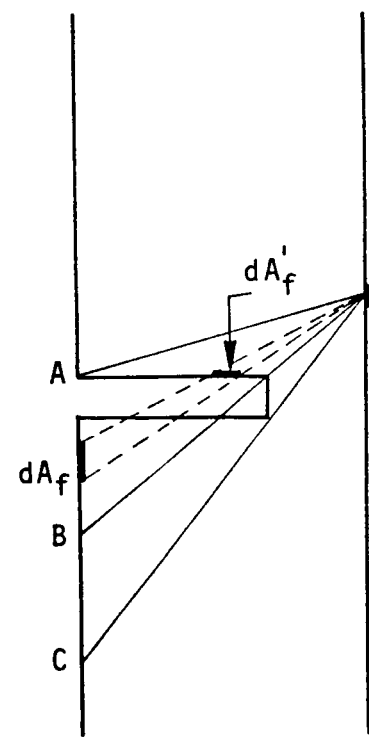


Fig. A-3: Radiation Solid Angles

$$\theta_{f,1} = \theta_n + \sin^{-1}(R_n/R_f) - \pi/2, \quad (\text{A-17})$$

$$\theta_{f,2} = \theta_n - \sin^{-1}(R_n/R_f) + \pi/2. \quad (\text{A-18})$$

Finally, as suggested by Figure A-3,  $z_{f,1} = -\infty$  and  $z_{f,2} = +\infty$ . Since  $\Omega_1$  is constant and  $\Omega_3$  changes only with vertical distance, Equation (A-13) is rearranged to:

$$q_{A_f \rightarrow A_n} = \Omega_1 \int_{z_{f,1}}^{z_{f,2}} \int_{z_{n,1}}^{z_{n,2}} \Omega_3 \int_{\theta_{n,1}}^{\theta_{n,2}} \int_{\theta_{f,1}}^{\theta_{f,2}} \Omega_2 d\theta_f d\theta_n dz_n dz_f. \quad (\text{A-19})$$

The result of the innermost integration, as suggested by Figure A-4, cannot be a function of  $\theta_n$ . Also, since  $\theta_{n,2} - \theta_{n,1} = \pi$ , and  $\Delta z_n$  is small such that:

$$\int_{z_{n,1}}^{z_{n,2}} \Phi dz_n = \Delta z_n \Phi, \quad (\text{A-20})$$

it follows that:

$$q_{A_f \rightarrow A_n} = \Omega_1 \Delta z_n \int_{z_{f,1}}^{z_{f,2}} \Omega_3 \int_{\theta_{f,1}}^{\theta_{f,2}} \Omega_2 d\theta_f dz_f. \quad (\text{A-21})$$

Using the transformation  $\theta_f - \theta_n = \eta$ , the innermost integral is transformed to the following form:

$$\int_{\theta_{f,1}}^{\theta_{f,2}} \Omega_2 d\theta_f = \int_{\eta_1}^{\eta_2} \frac{a \cos^2 \eta + b \cos \eta + c}{(d \cos \eta + e)^2} d\eta = \Gamma(z_n, z_f), \quad (\text{A-22})$$

where:

$$a = c = d/2 = -R_n R_f , \quad (A-23)$$

$$b = R_n^2 + R_f^2 , \quad (A-24)$$

$$e = R_n^2 + R_f^2 + (z_f - z_n)^2 , \quad (A-25)$$

$$\eta_1 = \sin^{-1}(R_n/R_f) - \pi/2 , \quad (A-26)$$

$$\eta_2 = -\sin^{-1}(R_n/R_f) + \pi/2 . \quad (A-27)$$

It is clear that, for constant  $R_n$  and  $R_f$ , the integral (A-22), denoted by  $\Gamma(z_n, z_f)$ , is a function of the axial locations  $z_f$  and  $z_n$  only. Taking  $R_n=5$  and  $R_f = 17.5$ , the integral (A-22) is solved numerically using the trapizoidal rule and the results are plotted in Figure A-5 for different values of  $z_n$  and  $z_f$ . It is found that all the curves in Figure A-5 can be accurately duplicated by the single function  $a_1 \operatorname{sech}(a_2 x)$  where  $x$  is equal to  $z_f - z_n$ . The constants  $a_1$  and  $a_2$  are, of course, functions of  $R_n$  and  $R_f$ . For the values of  $R_n$  and  $R_f$  given above,  $a_1$  and  $a_2$  are found to be 0.0086 and 0.153, respectively. Equation (A-21) can now be rewritten as:

$$q_{A_f \rightarrow A_n} = a_1 \Omega_1 \Delta z_n \int_{z_{f,1}}^{z_{f,2}} \Omega_3 \operatorname{sech} a_2(z_f - z_n) dz_f . \quad (A-28)$$

The above integral must be evaluated numerically for each  $A_n$  which denotes a cylindrical surface area associated with a certain boundary node. By choosing  $R_n$ , the area  $A_n$  can be positioned anywhere between the alloy's surface and the glass-air interface. In Equation (A-28),  $z_n$  is the axial location of the centroid of  $A_n$  which coincides with the axial location of the associated node. The limits  $z_{f,1}$  and  $z_{f,2}$  can be

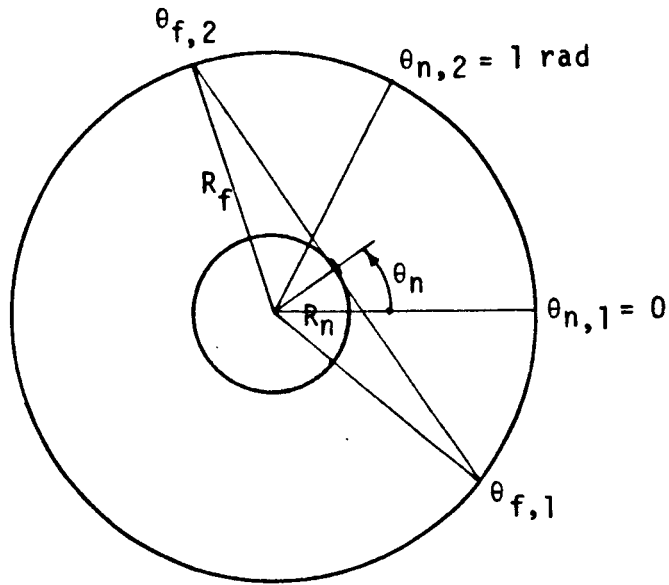


Fig. A-4: Radiation Geometry

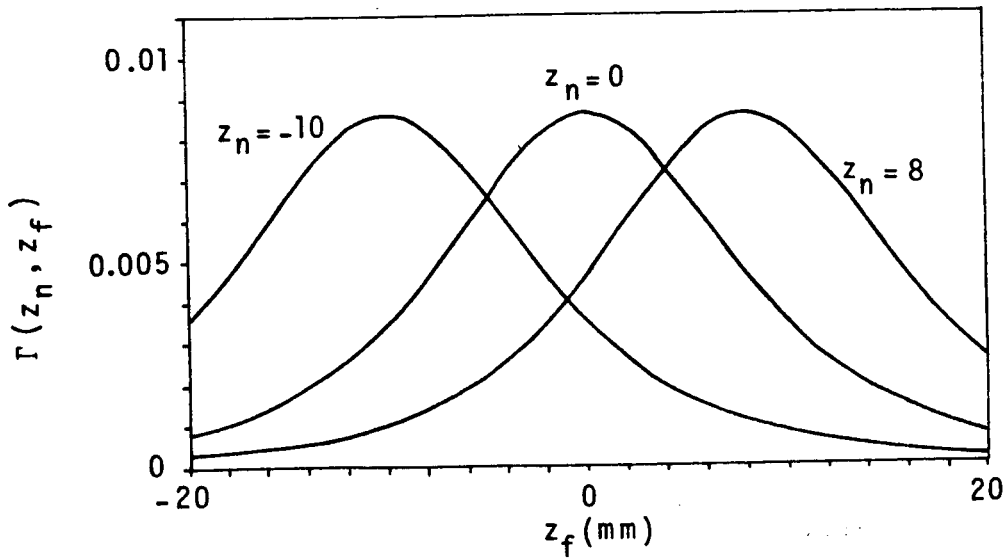


Fig. A-5: Radiation Mathematics

taken as large negative and large positive values respectively instead of  $-\infty$  and  $+\infty$ . This is possible because  $\Gamma(z_n, z_f)$  diminishes at a fast rate as  $z_f - z_n$  increases.

The integral (A-28) can be evaluated numerically by dividing the region  $(z_{f,1} \rightarrow z_{f,2})$  into a large number of elements with height  $\Delta z_f$  and centers at a variable  $z_f$ . The integral (A-28) takes the following discrete form:

$$q_{A_f \rightarrow A_n} = a_1 \Omega_1 \Delta z_n \Delta z_f \sum_{z_f} \Omega_3 \operatorname{sech}[a_2(z_f - z_n)] \quad (A-29)$$

Finally, the radiation flux in the vicinity of the node is obtained by dividing  $Q_{A_f \rightarrow A_n}$  by the area  $A_n$ :

$$Q_r = q_{A_f \rightarrow A_n} / A_n \quad (A-30)$$

By positioning  $A_n$  at the middle of the glass wall, the above  $Q_r$  becomes representative of an average heat flux exchanged between the furnace and the ampule by radiation.